

Laser-Annealing of Thermoelectric $\text{CuFe}_{0.98}\text{Sn}_{0.02}\text{O}_2$ Films Produced by Powder Aerosol Deposition Method

Tobias Nazarenus,* Jaroslaw Kita, Ralf Moos, and Jörg Exner

Powder aerosol deposition (PAD) is a unique coating method that allows the fabrication of dense ceramic films on a variety of substrates at room temperature. This spraying process can produce film thicknesses of several micrometers within minutes without the use of binders or other liquids. Although the functional properties of the well-adhering films are already present in the as-deposited state, the functional film properties are often reduced by several orders of magnitude. To recover bulk-like values, the samples are typically thermally post-deposition-treated in a furnace. In contrast, in this work, the films are locally annealed by a frequency-tripled Nd:YAG laser ($\lambda = 355$ nm). A thermoelectric material, doped copper delafossite, is sprayed via PAD and the influence of frequency-tripled Nd:YAG laser irradiation on the electronic and morphological film properties is investigated in detail. A very thin, glass-like surface layer forms whose electronic conductivity is three orders of magnitude higher than in the as-deposited state. This is proven by electrical impedance spectroscopy, microscopic images, and FEA-simulations.

1. Introduction

A new coating technology for ceramic thick films, which is becoming increasingly interesting for industrial applications, is the so-called Powder Aerosol Deposition Method (PADM or PAD).^[1] Due to the worldwide development of this process method, different names like aerosol deposition (AD),^[2] vacuum kinetic spray (VKS),^[3] vacuum cold spray (VCS),^[4] granule spray in vacuum (GSV), or nanoparticle deposition system (NPDS)^[5] are used by different research groups. The variety of suitable ceramics ranges from insulator materials like Al_2O_3 ,^[6] dielectric materials like BaTiO_3 and $\text{Bi}_4\text{Ti}_3\text{O}_{12}$,^[7] solid electrolytes for proton conducting fuel cells like $\text{Ba}(\text{Zr}, \text{Sn}, \text{Ce})\text{O}_3$,^[8–10] all-solid-state battery electrolytes like $\text{Li}_7\text{La}_3\text{Zr}_2\text{O}_{12}$,^[11] sensor materials^[12] and lunar regolith^[13,14] for futuristic applications in space to thermoelectric films like CuFeO_2 .^[15] Thermoelectric materials enable the direct emission-free conversion

of thermal to electrical energy and vice versa. The state-of-the-art material for thermoelectric generators (TEG) is bismuth telluride (Bi_2Te_3); however, its application is limited due to its high costs and tendency to oxidize at elevated temperatures. Copper-iron-oxides are a thermally stable promising alternative due to the low costs of the raw materials, their high Seebeck coefficient, and their high electrical conductivity.


The PAD method enables to form dense nanocrystalline ceramic films on a variety of substrates with high deposition rates.^[16–18] In contrast to all other ceramic processing routes, even moisture-sensitive ceramics, or ceramics with high sintering temperatures can be fabricated at room temperature (RT).^[11] Besides the dry ceramic powder, neither additional binders nor other liquids are needed. The ceramic particles are accelerated

towards a substrate by a pressure difference. The kinetic energy of the particles is converted into bonding energy during their impact on the substrate and comes along with the reduction of the crystallite size and formation of microstrain within the atomic lattice.^[19–21] Particle fracturing occurs along the grain boundaries and within the grains generating temporarily unsaturated surface bonds that cause an excellent adherence of the particles.^[22]

Despite all the positive aspects of the powder aerosol deposition summarized in **Figure 1**, a major disadvantage in the as-deposited state that all PAD films have in common is the reduced electrical conductivity of the films. A thermal annealing step is necessary to reduce the mechanical stress of the film and to restore the electrical properties so that they reach bulk values. Exner et al. recently found out that the required annealing temperature in the furnace depends on the melting point of the functional ceramic materials, though it is significantly lower than the typical sintering temperatures.^[23] In contrast, laser-based annealing could provide additional advantages like a reduced annealing time or a targeted local property change as it was shown by Palneedi et al. for PZT ($\text{Pb}(\text{Zr}, \text{Ti})\text{O}_3$)^[24–30] and Shinonaga et al. for TiO_2 .^[31–33]

In this study, we investigated the influence of laser irradiation on the properties of a nanocrystalline thermoelectric film. Tin doped copper-iron-oxide respectively copper delafossite ($\text{CuFe}_{0.98}\text{Sn}_{0.02}\text{O}_2$), which is known for its good thermoelectric properties and is processability by PAD,^[15,34] was synthesized by the mixed-oxide-route. Films were fabricated by powder aerosol deposition method. After deposition, the films were annealed with a frequency tripled Nd:YAG laser ($\lambda = 355$ nm) and its influence on the microstructure and the electrical properties was examined by optical and electrical measurements.

T. Nazarenus, Dr. J. Kita, Prof. R. Moos, Dr. J. Exner
University of Bayreuth
Department of Functional Materials
Universitätsstraße 30, Bayreuth 95440, Germany
E-mail: Functional.Materials@Uni-Bayreuth.de

 The ORCID identification number(s) for the author(s) of this article can be found under <https://doi.org/10.1002/admi.202001114>.

© 2020 The Authors. Published by Wiley-VCH GmbH. This is an open access article under the terms of the Creative Commons Attribution License, which permits use, distribution and reproduction in any medium, provided the original work is properly cited.

DOI: 10.1002/admi.202001114

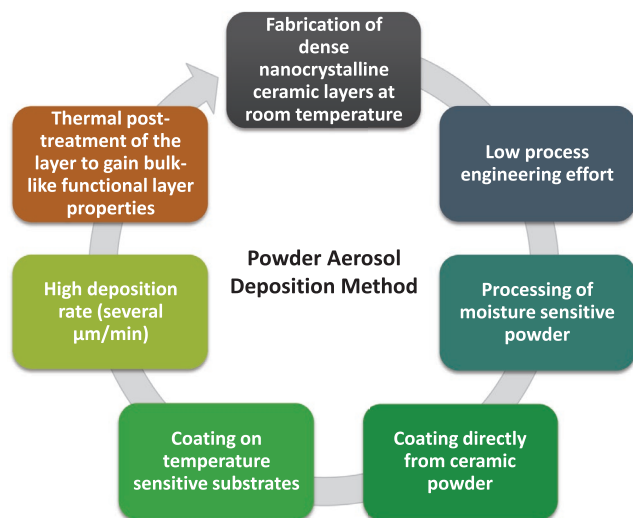


Figure 1. Characteristics of the powder aerosol deposition method.

2. Experimental Section

2.1. Powder Synthesis

$\text{CuFe}_{0.98}\text{Sn}_{0.02}\text{O}_2$ powder was synthesized by a mixed-oxide-route. The starting oxides Cu_2O (Alpha Aesar, 99 % purity), Fe_2O_3 (Alfa Aesar, 98 % purity) and SnO_2 (Alfa Aesar, 99.9 % purity) were mixed stoichiometrically and wet-ball milled in a planetary ball mill (Fritsch Pulverisette 5, Idar-Oberstein, Germany) with cyclohexane as milling fluid. The homogenization milling of the powder took place in a zirconia milling jar (which consists of ZrO_2 , stabilized with 3.5 wt% MgO) with zirconia milling balls (ZrO_2 , stabilized with 5 mol% Y_2O_3), for 4 h. After being homogenized, cyclohexane was removed in a rotary evaporator (Heidolph Instruments, Schwabach, Germany). The powder mixture was calcined at 1050 °C on quartz glass in a tube furnace (Carbolite, Neuhaus, Germany) in a mixed gas atmosphere of 1% O_2 in nitrogen for 12 h. In order to reduce the particle size to a suitable range for PAD, the powder was milled, dried and subsequently sieved with 90 μm meshes to remove large agglomerates. The powder then was stored at 200 °C for at least 48 h until it was used for PAD. Further details can be found in ref. [35].

2.2. Film Fabrication by Powder Aerosol Deposition

A custom-built PAD apparatus as shown in **Figure 2** was used. The apparatus consists of a vacuum pump to evacuate the deposition chamber and an aerosol generating unit. Oxygen was used as carrier gas. A flow rate of 6 L min^{-1} generated an aerosol and accelerated the particles through a slit nozzle (orifice size: $10 \times 0.5 \text{ mm}^2$) up to several hundred m s^{-1} by the pressure drop through the nozzle of ≈ 250 to 1 mbar at the deposition chamber. A dense ceramic $\text{CuFe}_{0.98}\text{Sn}_{0.02}\text{O}_2$ film was formed on the horizontally moveable substrate (5 mm s^{-1}) that was placed 2 mm from the nozzle.

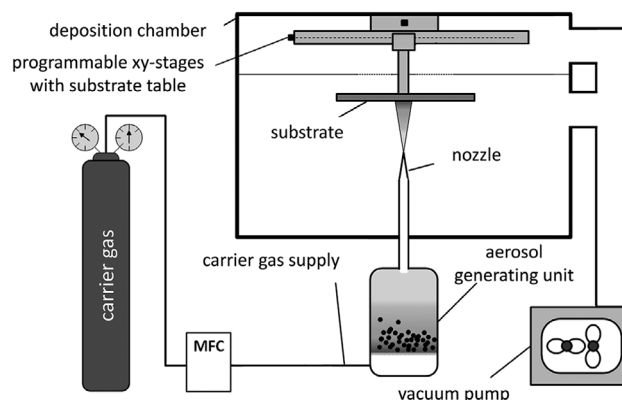


Figure 2. Schematic overview of the powder aerosol deposition apparatus.

2.3. Laser-Annealing of Powder Aerosol Deposited Films

The deposited films were laser-annealed by a frequency-tripled Nd:YAG laser ($\lambda = 355 \text{ nm}$) with a computer based positioning system (MicroLine 350L, LPKF Laser & Electronics, Garbsen, Germany) and a spot diameter in the focus of 20 μm . The laser was operated in a pulsed line scan mode where the opening frequency of the shutter was set to the maximum value of 40 kHz. To process the sample surface, the beam lines were placed side-by-side with an overlap of 5 μm referred to a spot diameter of 20 μm . The samples were placed 1.6 mm beneath the focus point to reduce the resulting energy density. The scan speed of the laser was set to 200 mm s^{-1} . This leads to area-specific annealing rates on the sample of $\approx 47 \text{ mm}^2 \text{ s}^{-1}$ for a single scan, while the number of scans, n , was varied. For an effective optical absorption, the photon energy (here 3.5 eV) has to be higher than the bandgap ($E_{\text{g, min, delafossite}} = 1.3 \text{ eV}$) of the CuFeO_2 according to Tauc's relation.^[36]

2.4. Mechanical, Crystalline, and Optical Analysis: SEM, XRD, and Profile Stylus

To optically analyze the films, they were sprayed onto alumina substrates. Cross-sectional images were captured by the scanning electron microscope Zeiss Leo Gemini 1530 VP (field emission cathode, inlens and secondary electron detector, operating voltage 3 kV) to observe the film morphology. The crystalline phase composition of the powder and the PAD film on alumina substrates was analyzed before and after the laser-annealing procedure by the X-ray powder diffractometer Bruker D8 Advance (Cu-Anode 2.2 kW, $\lambda = 1.5406 \text{ \AA}$, Ge-K $\alpha 1$ -monochromator, 1D-Lynxeye-detector) between 20° and 80° (2 θ) in steps of 0.02° for a hold time of 1 s. The reflex patterns were taken at room temperature. The film thickness was determined by a profile stylus instrument type Mahr Perthometer S2.

2.5. Electrical Impedance Measurement Setup

To determine the electrical film conductivity at room temperature, PAD films were deposited on screen-printed platinum

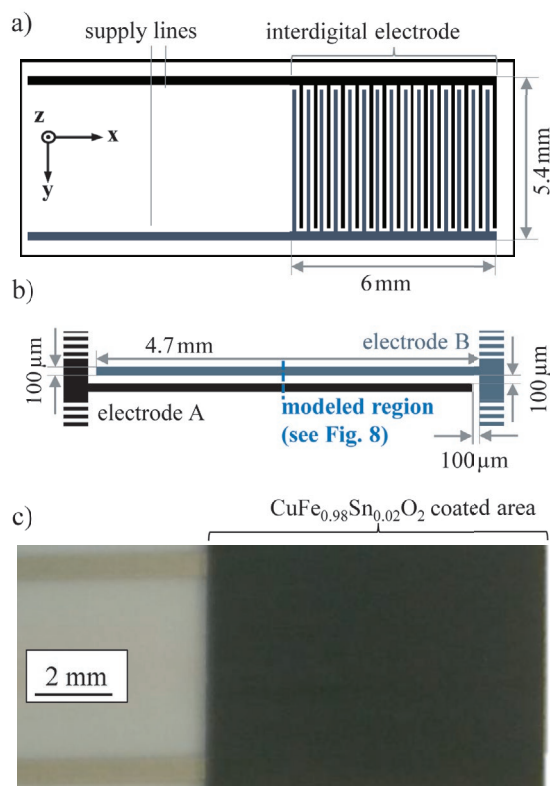


Figure 3. Samples used for impedance spectroscopy: a) design scheme of the platinum interdigital electrodes on an alumina substrate, b) geometry design of one prepetition unit of metallic fingers, magnified from a, c) image of $\text{CuFe}_{0.98}\text{Sn}_{0.02}\text{O}_2$ coated interdigital electrode.

interdigital electrodes (IDE) structures on alumina substrates (Rubalit 708S, CeramTec, Marktredwitz, Germany). The electrical field distribution of this electrode structure was also described in ref. [37]. For the electrical characterization on these samples, impedance spectroscopy measurements (IS, Novocontrol α -Analyzer, $f = 2$ MHz to 1 Hz, ac-signal amplitude $U_{\text{rms}} = 20$ mV) were conducted. The resulting spectra were fitted using the equivalent circuit $R||CPE$ by the software ZView (Scribner Associates, Inc., USA). **Figure 3** shows the electrode geometry (a) as complete structure, in detail for two adjoining electrode fingers (b), and as well as an image of the coated sample (c). The conductivity σ of the untreated film was calculated according to Equation (1) out of the fitted resistance R , whereas F is the geometry factor that is defined by Equation (2). It depends on the number of fingers ($m = 15$), the finger length ($l = 4.5$ mm), the finger width ($w = 100$ μm) and the spacing between the fingers ($d = 100$ μm):

$$\sigma = \frac{1}{R \cdot F} \quad (1)$$

$$F = \frac{(2m-1) \cdot l \cdot t + 2 \cdot m \cdot w \cdot t}{d} \quad (2)$$

All measurements were conducted at room temperature. The impedance of the films was measured between the laser-annealing steps.

2.6. Simulation of the Electrical Behavior

When using interdigital electrodes to determine material-specific values like the electrical conductivity, Equations (1) and (2) can only be applied under certain conditions:

- 1 the investigated film should be homogenous in terms of film thickness,
- 2 it features isotropic and homogeneous material properties (e.g., constant electrical conductivity throughout the complete film volume), and
- 3 it has a film thickness not significantly larger than the height of the electrodes (here, the limit is 10–20 μm)^[37]

As the laser-annealing may only treat certain regions close to the film surface, hence only affecting the properties in the upper part of the film, the assumption of a constant electrical conductivity throughout the film is no longer valid. To trace changes of the measured resistance to an altered electrical conductivity after annealing, a detailed computational modelling was conducted by finite element analysis. The AC/DC module of the COMSOL Multiphysics software was used to model the electrical potential and electric field lines on the interdigital electrode including coating, substrate and air. The 2D-model consisted of a cross-section of the sample, namely an alumina substrate, a pair of alternating platinum electrode fingers A and B, respectively, with a geometry according to Figure 3b, a film divided into one to four layers with adjustable electrical conductivity and thickness (different stages of the annealing procedure), and air. **Table 1** summarizes the materials and their parameters as required for the model. The modeled section had a width of 400 μm ($2 \times$ width of electrodes and $2 \times$ spacing between the electrodes) and a height of about 1650 μm . The height of the modeled PAD film was adjusted to the measured profile of the sample under test (see Figure 8a and Figure 12a as well as **Table 2** for details).

The following boundary conditions were applied to the model:

- Conservation of charge within the limits of the model
- Electrical insulation at the top and bottom limit of the model
- Electrode A was set to a potential of 50 mV
- Electrode B was the electrical ground
- A (continuous) cyclic symmetry condition on the left and right-hand side of the model

While the first four conditions are quite clear, the last condition may require a further explanation. Since the modeled section (or unit) of the sample (two electrode fingers, two spacings

Table 1. Materials and their properties used to model the electrical behavior.

Part	Material	Height [μm]	Conductivity [S cm^{-1}]	Permittivity
Substrate	Al_2O_3	635	10^{-8}	10
Electrode	Platinum	5	10^5	1
PAD film	$\text{CuFe}_{0.98}\text{Sn}_{0.02}\text{O}_2$	10–22	10^{-5} – 10^{-2}	200
Air	Ambient air	1000	10^{-14}	1

Table 2. Overview of the produced samples and conducted experiments.

Sample number	Substrate	Film thickness [μm]	Laser treatment	Analysis
I	Al_2O_3	5	Part (i): 0 scans Part (ii): 64 scans	XRD before and after annealing
II	Al_2O_3	$\approx 4-6$	Part (i): 0 scans Part (ii): 1 scan Part (iii): 32 scans	SEM images of the top view and the fractured cross section for all three stages
III	IDE on Al_2O_3	10	0/1/2/4/8/16/32/64/128 scans	IS @ RT in between laser-annealing
IV	Al_2O_3	First film: 18 Second film: 15	First film: 16 scans Second film: 16 scans	SEM image of a four-layer setup with two annealed surfaces post-mortem
V	IDE on Al_2O_3	First film: 12 Second film: 10	First film: 0/1/2/4/8/16 scans Second film: 0/1/2/4/8/16	IS @ RT in between laser-annealing for a single film and a two-film setup after a second deposition
VI	Al_2O_3	10	Part (i): 0 scans Part (ii): 1 scan Part (iii): 32 scans	EDX mapping

between the electrodes) was not isolated, but instead packed in between more of these units on both sides, the electrical potential was affected by the neighboring units. However, each unit featured an identical field distribution and course of electrical potential. As a direct consequence, the potential and the field distribution at the lateral boundaries of neighboring units had to be identical and therefore, due to symmetry, had to be identical at the left and right boundary of a single unit, too. This behavior could be modeled by the described cyclic symmetry condition. The resistance was then calculated by the number of units (14) and the electrode length. The film conductivity of the PAD film was modified until the calculated resistance from the simulation coincide with the measured resistance obtained by impedance spectroscopy. Using this computational method and the measurement procedure described in the next section, contributions of regions of the film with different electrical conductivities to the total resistance were distinguished.

3. Experimental Procedure

The film formation and the laser-annealing is depicted in Figure 4 and described in detail in this section. After the synthesis, the micrometer-sized ceramic particles were deposited onto substrates by the powder aerosol deposition method. Films on platinum electrodes were used for electrical characterization via impedance spectroscopy (IS), while XRD and SEM analysis were conducted on films on alumina substrates. Additionally, a second film on

an alumina substrate and on interdigital electrodes was sprayed and annealed according to Figure 4c,d for optical and impedance analysis. Mechanical, optical, and impedance measurements were carried out before, during (after defined annealing scans), and after the two annealing processes. For future applications in thermoelectric generators, alumina substrates might not be ideal due to their high thermal conductivity even at higher temperatures. Nevertheless, the used IDE structures on alumina were well suited to quantify the changes of electrical properties of the PAD films during the laser annealing steps. The findings can be transferred to other substrate materials.

Table 2 summarizes all produced samples with their thickness as well as the type of laser treatment and the conducted analysis. Additionally, an image of the as-deposited and the laser-annealed surface after different laser scans is provided in Figure S1, Supporting Information.

4. Results and Discussion

4.1. Crystalline and Morphological Changes of the PAD Films during Laser-Annealing

4.1.1. Phase Analysis

To address the crystal structure of the $\text{CuFe}_{0.98}\text{Sn}_{0.02}\text{O}_2$ after powder calcination and film deposition, XRD was conducted (sample I).

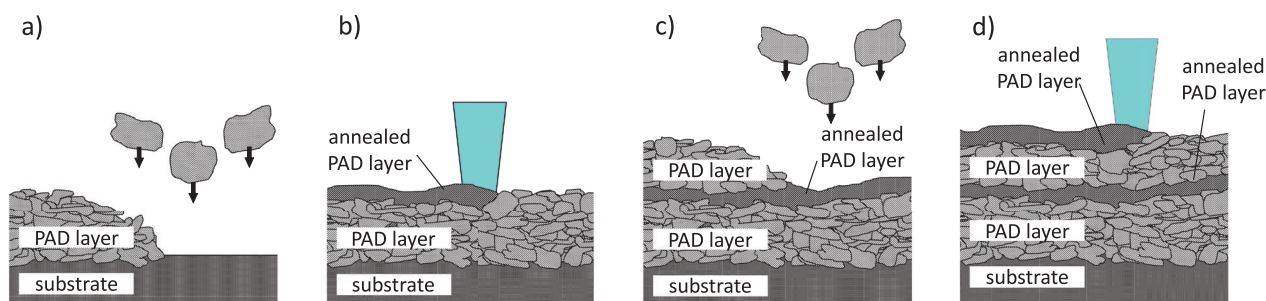


Figure 4. Process of film fabrication and laser-annealing: a) deposition of the ceramic particles on a substrate, b) laser-annealing of the surface layer, c) second deposition of ceramic particles on the annealed film surface, d) laser-annealing of the second film.

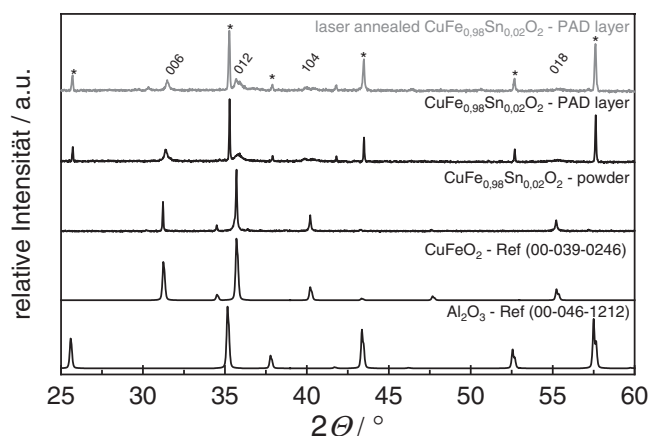


Figure 5. XRD pattern of the synthesized $\text{CuFe}_{0.98}\text{Sn}_{0.02}\text{O}_2$ powder and the PAD film on an alumina substrate in the as-deposited state and after the laser-annealing compared to the references. Reflexes of the substrate are marked by an asterisk.

Figure 5 shows the XRD pattern of the synthesized powder and additionally of the therefrom sprayed PAD film. Diffraction patterns of the PAD film on the alumina substrate taken before and after the laser-based treatment with 64 scans are shown as well. The pattern of the uncoated alumina substrate as well as reference pattern of CuFeO_2 (ICDD 00-039-0246) are added for comparison.

The reflections at 31.2° (006), 35.7° (012), 40.2° (104), and 55.2° (018) of the calcined powder clearly match the CuFeO_2 delafossite phase in terms of relative reflex intensities and reflex positions.^[38] The Sn-doping in the present amount of 2 mol% does not affect the lattice constants and therefore the XRD pattern.^[39] Based on the reflex pattern of the PAD film in the as-deposited state, a successful film formation can be concluded. Next to the sharp reflexes that belong to the alumina substrate beneath the film, broadened reflexes of the PAD film are present. The penetration depth of the X-ray radiation can reach up to 10 μm depending on the investigated material. Hence, also information about the substrate (alumina) are found in the resulting reflex pattern for thin film thicknesses. The reflex broadening of the PAD film material is the result of the room temperature impact consolidation (RTIC) mechanism. Caused by this deposition mechanism, the ceramic particles with sufficiently high kinetic energy get fractured, form a nanocrystalline film and additionally consolidate the previously deposited particles through the hammering effect.^[20] As it is reported in literature by Schubert et al., these films are under high compressive stresses owing to the impact-based film formation.^[40] The broadened reflexes remain unaffected by the laser-annealing of the film. The results are in contrast to findings in literature, according to which furnace-annealing with moderate heating and cooling rates as well as long dwell times leads to a reduction of the reflex widths and hence to grain growth at higher temperatures.^[3,10,11,23,41] The observed phenomenon can be explained by high heating and cooling rates caused by the laser that may lead to a glassy microstructure. However, a glassy microstructure cannot be detected by XRD analysis. Despite laser-annealing in air, no further

reflexes in the annealed PAD film are present, indicating that the PAD film is single-phased in both, the as-deposited and the laser-annealed state as reported in literature.^[42]

4.1.2. Scanning Electron Microscopy

The influence of laser-annealing on the morphology of CuFeO_2 PAD films (sample II) is examined by SEM. **Figure 6** shows the top view and the fractured cross section of the 4–6 μm thick films in the as-deposited state (Figure 6a,b), as well as after one scan of the laser beam (Figure 6c,d) and after 32 consecutive scans (Figure 6e,f). All fractured cross-section images indicate the strong bond of the PAD film to the alumina substrate, which is typical for the RTIC deposition mechanism.^[43,44]

The homogeneous film in Figure 6a represents the typical surface structure of a powder aerosol deposited film with shallow craters that are caused by the particle bombardment.^[45,46] In the high magnification inset of the top view as well as in the fractured cross section (Figure 6b), the nanocrystalline sized fragments can be observed that result from the RTIC mechanism. The nanometer-sized grains are in direct contact to the substrate and form a dense film. During the impact, an amorphization of the particle surface may take place; however, this cannot be detected by SEM or XRD.^[4] Due to the impact-based film formation, nanometer-sized pores are plausible. While a high film density is evident, the fractured cross-section does not allow for a quantitative statement on the actual porosity. Nevertheless, it is well known that PAD films are gas tight.^[17] Compared to the as-deposited film, the surface morphology changes already when only one laser scan ($n = 1$) is applied. The top view of the surface (Figure 6c) shows a partially melted surface. It can be concluded that the local temperature on the film surface clearly exceeds the melting temperature of around 1180 $^\circ\text{C}$. Due to the high scan speed and consequentially the high heating and cooling rates, the surface is not fully covered by rapidly solidified melt. Furthermore, the high local temperature decreases both the nano-porosity and the nano-roughness of the surface film. The ultraviolet laser wavelength primarily affects the film surface and reaches about 1 μm deep as it is visible in Figure 6d. Also, the surface quality is increased by the leveling of small bumps. Since the laser only treats the top micrometer near the surface, the interface between the film and the substrate after a single scan remains unaffected and is similar to the as-deposited sample (Figure 6b). In Figure 6e, micro-cracks on the surface of a $\text{CuFe}_{0.98}\text{Sn}_{0.02}\text{O}_2$ film after 32 scans occur owing to the continuous melting and solidification with high temperature gradients. These cracks can mainly be found in the annealed layer and do not penetrate the film in the as-deposited state. The total area that is less affected by the laser on the surface is clearly reduced by the higher number of scans. While the low magnification top view makes the vertical pulsed line scan mode of the laser movement apparent (indicated by the yellow dashed lines), a significantly modified surface is visible in high magnification insets. The nanocrystalline appearance is converted into a flattened surface with pronounced low nano-porosity. Due to the higher energy intensity in the middle of

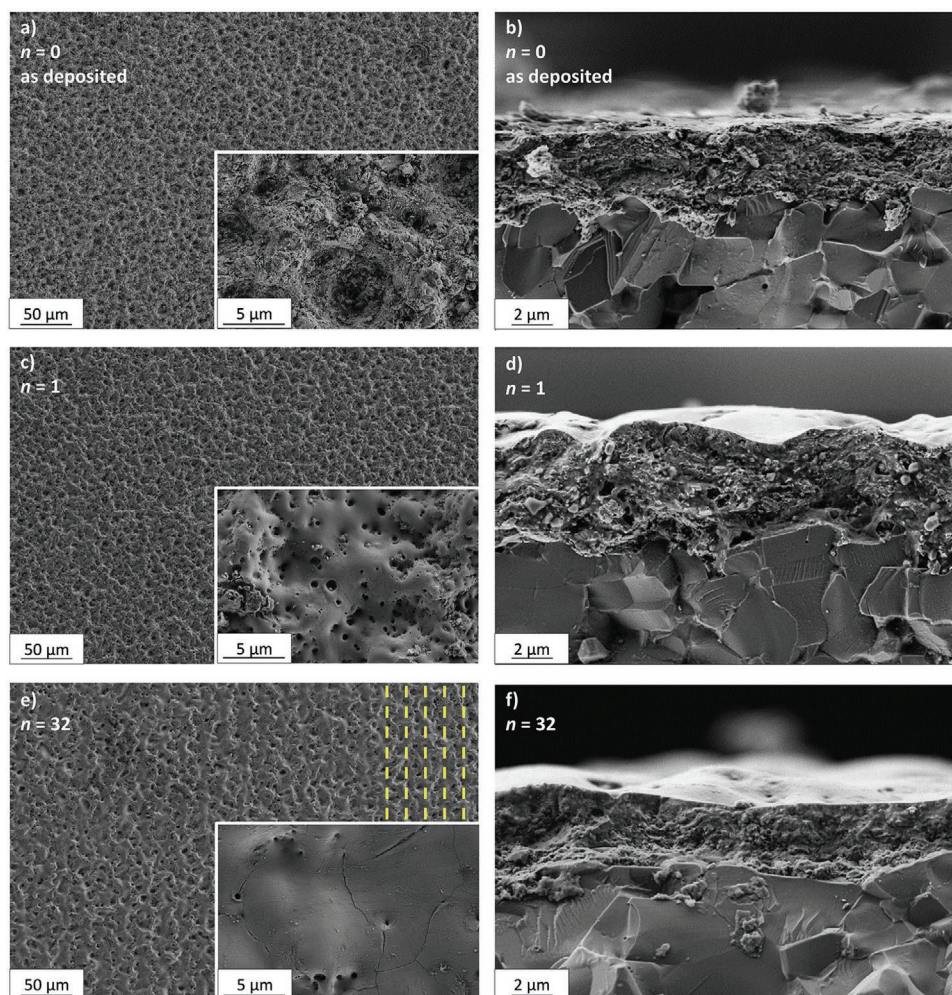


Figure 6. SEM images of the $\text{CuFe}_{0.98}\text{Sn}_{0.02}\text{O}_2$ PAD films on alumina substrates in the as-deposited state: a) top view and b) fractured cross-section; after a single laser scan ($n = 1$): c) top view and d) fractured cross-section; after 32 laser scans ($n = 32$): e) top view with yellow lines that indicate the vertical laser movement and f) fractured cross section. Insets show details with higher magnification.

the laser spot, the annealing is not completely homogeneous within the entire area. An increased overlap of the laser beam lines during the scans may provide a more homogeneous surface treatment. On the basis of Figure 6f, it can be stated that the depth of the annealed surface does not change when the number of scans increase, whereas the affected surface area changes. It can be estimated that the results that are shown in Figure 6e,f can also be generated by an increased overlap of the laser beam and an decreased number of scans. The homogeneous thermal annealing in a furnace in contrast does not significantly change the microstructure of a PAD film due to significantly lower process temperatures,^[11] whereas during the laser treatment the temperature increases above the melting point. The high local temperatures that even lead to a partial melting of the CuFeO_2 film may also cause a phase segregation. To investigate whether a phase segregation occurs, EDX mappings of as-deposited and laser treated films were prepared (shown in Figures S2–S4, Supporting Information). Even after a high number of 32 laser scans, the element distribution is still homogeneous and therefore the occurrence of phase segregations can be neglected.

4.2. Influence of the Laser-Annealing on the Electric Conductivity

4.2.1. Electrical Resistance of a CuFeO_2 Film

The electrical resistance of a 10 μm thick CuFeO_2 PAD film (sample III) on platinum IDE was measured in its as-deposited state and after laser-annealing for 1 to 128 scans. Impedance spectroscopy according to section 2.5 quantified the influence of laser-annealing on the electrical resistance of the thermoelectric films. Sample III was measured in the as-deposited state directly after the coating process and after n laser scans. The samples were processed as depicted in Figure 4b. The impedance data in dependency to the number of laser scans are shown in the Nyquist plots in Figure 7a,b. Furthermore, the software-based calculated resistance, R , assuming a $R||CPE$ equivalent circuit, is shown in Figure 7c.

All spectra consist of a (partially flattened) semicircle, representing the electrical resistance and capacitance of the film. A differentiation into a grain and a grain boundary contribution is not possible, as already observed for ionically conducting

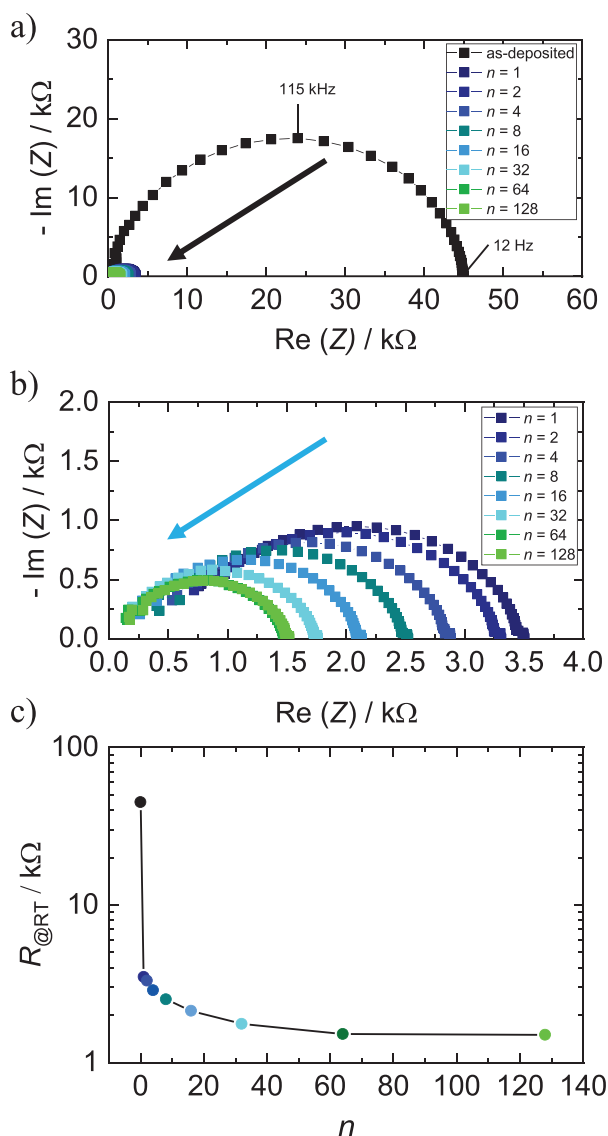


Figure 7. Relation between the number of laser scans n and the electrical impedance of the 10 μm thick $\text{CuFe}_{0.98}\text{Sn}_{0.02}\text{O}_2$ PAD film measured at room temperature: a) impedance data represented in a Nyquist plot, b) magnification for $n \geq 1$ and c) resistance R at room temperature as it depends on the number of laser scans n .

PAD films on IDE.^[21] Already after the first laser scan, the resistance drops significantly from 45 k Ω in the as-deposited state to 3.5 k Ω (for $n = 1$). With a rising number of laser scans, the resistance decreases continuously and asymptotically approaches a minimum value of 1.50 k Ω after 128 scans. Because of the small difference between the resistance after 64 scans (1.52 k Ω) and after 128 scans, we do not expect a further decrease of the resistance at even higher numbers of scans.

When it is considered that the laser beam primarily affects the surface to a depth of around 1 μm , we suggest that there is a two-layer setup within the annealed film: An upper, laser-treated, highly conductive layer and a second layer beneath that is not or almost not influenced by the laser beam and therefore has the conductivity of the as-deposited state. Since the

IS measurements do not allow to separate the contributions of the two layers, the conductivity of the highly conductive surface layer is calculated using a simulation model.

4.2.2. Modeling of the Electrical Film Behavior (Two-Layer Model with a Highly Conductive Surface Layer)

Based on the observation from SEM images (Figure 6) and impedance data (Figure 7), a two-layer simulation model is used to describe the electrical behavior in detail. At first, the as-deposited state without an annealed surface layer is simulated. The conductivity of the as-deposited film of $1.67 \cdot 10^{-5} \text{ S cm}^{-1}$, which is calculated by Equations (1) and (2) for the measured film thickness of 10 μm , has the same order of magnitude as polycrystalline films reported in literature.^[47] The software-based calculated conductivity coincides with this value, also proving that the simulation is correct. The geometry of the 2D model consisting of electrodes and the film in the as-deposited state with a homogeneous conductivity is shown in Figure 8a. In Figure 8b, the corresponding field distribution is shown for only one electrode, since field lines are symmetrical for the utilized electrode setup.

For the two-layer model four assumptions are made:

- 1 Laser-annealing only effects the upper surface layer with 1 μm thickness. By laser-annealing, the electrical conductivity σ of this layer volume is altered.
- 2 The overall film thickness remains constant during laser-annealing.
- 3 The conductivity σ of the 9 μm thick bottom layer remains constant during laser-annealing and is identical to the as-deposited state ($\sigma_{\text{as-deposited}} = 1.67 \cdot 10^{-5} \text{ S cm}^{-1}$).
- 4 The overall measured resistance consists of contributions from the two different layers with different conductivities.

The conductivity of the surface layer is varied until the simulated overall resistance is equal to the measured overall resistance from Figure 7c. For as-deposited film, the field lines are nearly parallel in between the electrodes, visible on the left-hand side of electrode B for $x < 250 \mu\text{m}$ in Figure 8b. A large area of the film in this region is permeated by field lines originating from the 5 μm high vertical boundary of electrode B. In contrast, field lines from the 100 μm wide horizontal electrode boundary first bend about 90° counterclockwise and are subsequently mainly located at the top of the film near the surface for $x < 250 \mu\text{m}$. In Figure 8c, the simulated two-layer setup is exemplarily shown for 8 scans. Because laser-annealing forms a highly conductive surface layer, the field line distribution significantly changes compared to the as-deposited state in Figure 8b. Now, field lines above the electrode B barely bend and are initially oriented nearly vertical in the unannealed lower layer up to the boundary of the highly conductive annealed surface layer. Here, field lines strongly bend counterclockwise. The majority of field lines points towards the annealed layer, even field lines originating from the vertical boundary of the electrode. Therefore, by surface annealing the upper layer of a PAD film on interdigital electrodes, the course of field lines in between the electrodes A and B is changed strongly: from nearly parallel, homogeneously distributed over the complete volume in the as-deposited state to highly focused to the surface layer after laser-annealing.

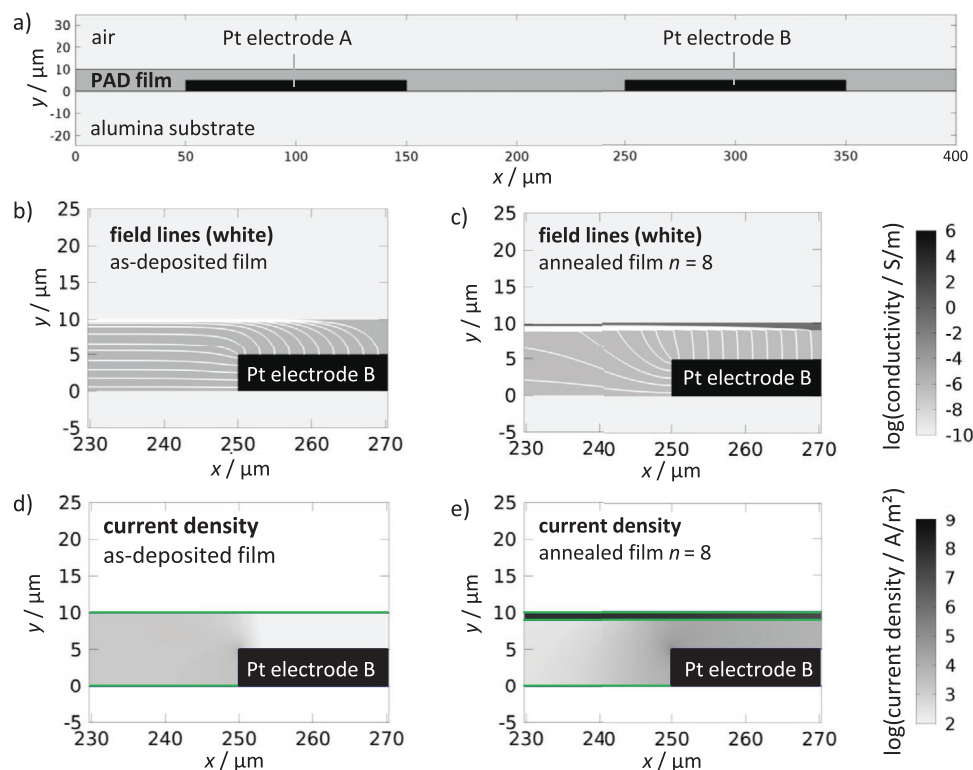


Figure 8. Modelling of the electrical behavior of a 10 μm thick PAD CuFeO_2 film on interdigital electrodes: a) used 2D geometry consisting of an alumina substrate, a pair of interdigital electrode fingers of platinum, the PAD film and air; field line distribution near electrode B for b) an as-deposited PAD film and c) an annealed PAD film ($n = 8$); current densities in the identical region for d) an as-deposited PAD film and e) an annealed PAD film ($n = 8$) with green lines marking the boundaries of electrode and layers.

The described behavior can be clearly seen when comparing the current densities for both stages (Figure 8d,e). For the as-deposited state, the region above electrode B ($x > 250 \mu\text{m}$, $y > 5 \mu\text{m}$) exhibits a very low current density (displayed in a logarithmical scale for better visibility) and therefore hardly participates in the transportation of charge carriers. The current flows mainly in the region between the electrodes with $x < 250 \mu\text{m}$ with a moderate current density. When a highly conductive surface layer is present, even if it is only 1 μm in thickness, a completely changed behavior occurs. The current density between the electrodes in the unaffected region (lower layer, $x < 250 \mu\text{m}$, $0 < y < 9 \mu\text{m}$) remains at a moderate level; however, the annealed surface layer causes the low resistance. Since the distance between the horizontal electrode boundary and the annealed film is just 4 μm , an increased current density occurs above the electrode, connecting the electrode and the conductive layer.

The simulation enables the separation of the overall resistance into contributions from each of the two layers. The calculated conductivity of the surface layer in dependency of the number of laser scans is shown in Figure 9. Based on the simulation, the surface layer conductivity is increased by nearly three orders of magnitude. Already after one laser scan, the conductivity increases to $2.3 \cdot 10^{-3} \text{ S cm}^{-1}$. After 128 scans a maximum conductivity of $10.3 \cdot 10^{-3} \text{ S cm}^{-1}$ is archived. The positive effect of a thermal annealing in a furnace on the electric properties of various electrically conductive functional PAD films after the

deposition process has recently been reported. One reason for the increase of the conductivity is the reduction of strain within the film.^[23]

On the one hand, the conductivity of the PAD surface layer after laser-annealing is still reduced compared to the

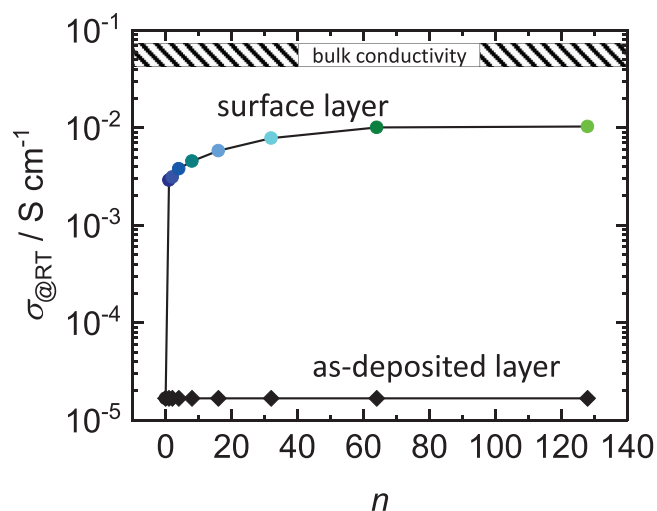


Figure 9. Calculated conductivity of the surface layer and the bottom layer in dependence of the number of scans n compared to bulk samples from ref. [15].

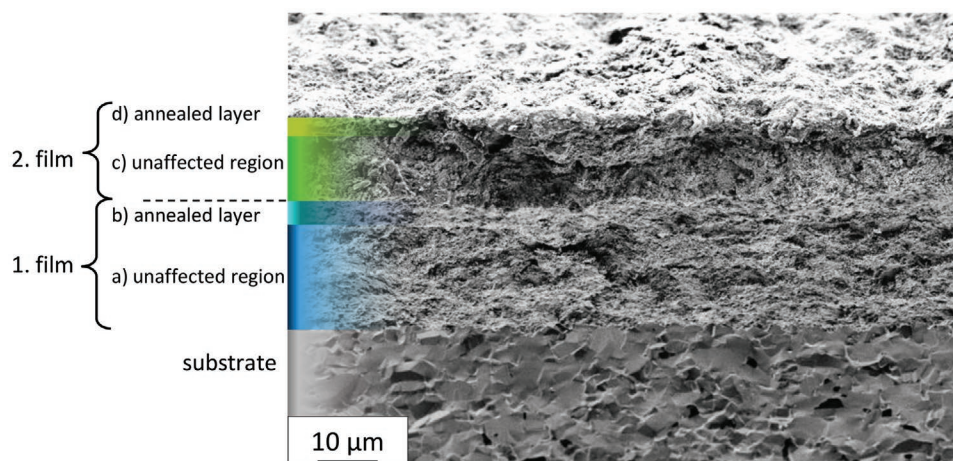


Figure 10. SEM image of a $\text{CuFe}_{0.98}\text{Sn}_{0.02}\text{O}_2$ film in a four-layer setup: the second film was deposited and laser-annealed on a first film that had been laser-annealed after its deposition. The different layers are indicated with different colors on the left side as a guide for the eye. Additional images are provided in Figure S5, Supporting Information.

conductivity of bulk samples in literature ($\sigma_{\text{bulk}} = 0.06$ to 0.09 S cm^{-1}).^[15] On the other hand, the conductivity of the surface layer is close to a CuFeO_2 PAD film that was annealed in a furnace at 900°C ($\sigma_{\text{CuFeO}_2, \text{ref}} = 0.03 \text{ S cm}^{-1}$) and sol-gel dip-coated films after an annealing at 800°C for at least 1 h.^[15,48] When the microstructure of the surface layer is taken into account, the microcracks might lower the conductivity. As it was already shown in Figure 6, laser-annealing is not completely homogeneous since the radiation power of the laser is not constant over the beam diameter and also the overlapping area of the laser beam has to be considered. Therefore, it is possible that also within the surface layer areas with different conductivities exist.

Analogously to the results of Palneedi et al., who have intensively investigated the influence of laser irradiation on PAD films of PZT ($\text{Pb}(\text{Zr,Ti})\text{O}_3$), we can show that the energy of the UV laser is primarily absorbed in a $\approx 1 \mu\text{m}$ thick surface layer.^[30] The functional properties of the PZT films were significantly increased by heat treatments with different lasers.^[24–29] Furthermore, Shinonaga et al. investigated the positive influence of laser irradiation on the functional properties and the microstructure on TiO_2 PAD films.^[31–33]

When this type of laser with a relatively low penetration depth should be used to anneal thicker films ($>1 \mu\text{m}$), it is necessary that the film production and the laser-annealing repeatedly alternate.

4.2.3. Multilayer PAD Film with Multiple Laser-Annealing Steps

If not just the first $1 \mu\text{m}$ of the film should be annealed but a large volume (or ideally the total film thickness), the laser-annealing procedure has to be conducted multiple times during the film growth. This means PAD and laser-annealing are operated alternately, most effectively after the deposition of an additional film thickness of one micrometer. As a proof of concept, a sample consisting of two stacked PAD films is prepared, where each film is laser-annealed after its deposition. The produced sample consists the total of four different layers, namely:

a) unaffected bottom layer of the first film, b) laser-annealed layer of the first film, c) unaffected lower layer of the second film, and d) the laser-treated surface layer. The procedure is according to Figure 4c,d.

In order to investigate the morphology, **Figure 10** shows an SEM image of these four layers on an alumina substrate (sample IV). In this case, the first film has a thickness of $\approx 18 \mu\text{m}$ after deposition and $1 \mu\text{m}$ micrometer is annealed at the surface during laser-annealing. The second film was deposited onto the annealed film. It has an additional thickness of $\approx 15 \mu\text{m}$, whereas also $1 \mu\text{m}$ micrometer is thermally annealed by the laser beam.

The second film adheres well onto the first film, even with its laser-annealed surface. The PAD films can be easily distinguished in the SEM images and the annealed areas are identified due to their changed microstructure, which already has been described earlier.

According to the process sequences shown in Figure 4, the impedance of a sample on IDE was measured during different stages of its production (sample V). The influence of laser-annealing on the films with the thicknesses of $12 \mu\text{m}$ (first film) and $10 \mu\text{m}$ (second film) is quantified by the impedance spectra shown in **Figure 11**. Figure 11a,b shows the impedance spectra of the first film in the as-deposited state as well as in dependence of the number of laser scans. All measurements show semi-circles as already observed for sample III. Due to the increased thickness, the total resistance of the as-deposited film (sample V) of $R = 25 \text{ k}\Omega$ is smaller than for sample III. With increasing numbers of laser scans, the resistance drops to $2.4 \text{ k}\Omega$ after a single scan and to $1.4 \text{ k}\Omega$ after 16 scans. In Figure 11c, the impedance spectra after the second film deposition are shown after different numbers of laser scans. Figure 11d summarizes the measured resistances as a function of the number of scans.

Annealing of the first film confirms the previous results. The first laser scan leads to a significant decrease of the resistance and the resistance decreases asymptotically with subsequently increasing number of scans, n . After 16 laser scans, the second film was deposited onto the annealed surface. Despite

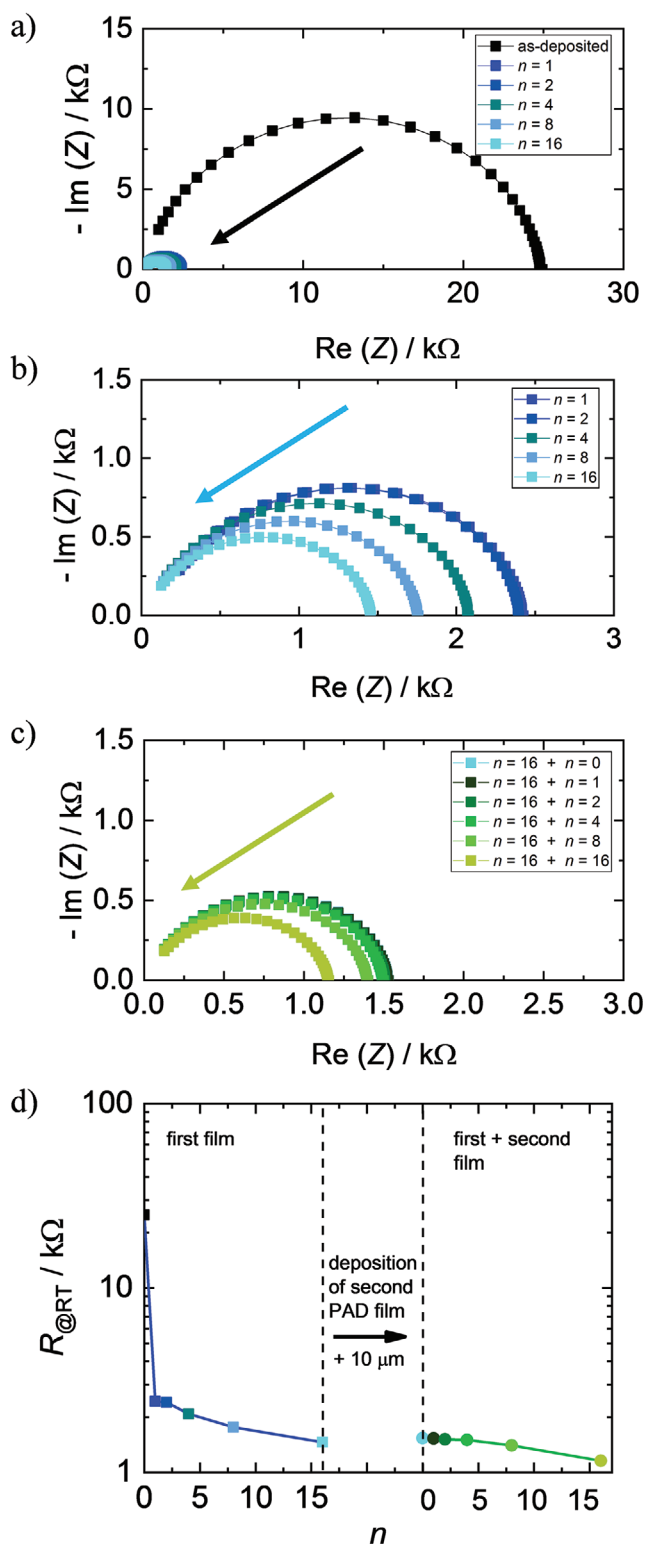


Figure 11. a) Overview of all impedance data of the $\text{CuFe}_{0.98}\text{Sn}_{0.02}\text{O}_2$ film after different numbers of scans of the first film, b) magnification of the impedance data at higher numbers of scans n for the first film, c) impedance data after applying the second film before and after laser-annealing for different numbers of scans, d) dependency of the calculated resistance on the number of scans, n .

the higher film thickness, the resistance increases from 14.6 k Ω to 15.3 k Ω directly after the second deposition without a surface treatment. This is in contrast to the assumed behavior according to which the electrical resistance should decrease with increasing film thickness. The reason might be the following: The measurement results indicate a reduction in thickness of the highly conductive laser-treated surface film. PAD is based on an abrasion and deformation of the substrate surface, as it was observed by various groups, mostly described as a formation of an anchoring layer.^[49–51] The same may happen to the annealed surface of the first film when depositing the second film. When also the second film is annealed by the laser, the resistance decreases further as shown in Figure 11c,d.

4.2.4. Simulation of the Electrical Behavior using a Four-Layer Model

In order to quantify the reduction of the annealed surface layer thickness after applying the second film, the simulation was extended to a three- and four-layer model. In the model, a highly conductive surface layer separates the first and the second unannealed film (Figure 12a).

As shown in Figure 12b, the second film barely influences the field line distribution whereas the annealed layer (Figure 10 region b) between both unaffected layers (Figure 10 regions a and c) dominates the total resistance. The majority of field lines is located within the thin yet highly conductive annealed layer (Figure 10 region b). The thickness of this intermediate layer is varied until the simulation matches the measured resistance data of $R = 15.3 \text{ k}\Omega$. Based on the assumption that the conductivity of the untreated part of the layers ($\sigma = 1.61 \cdot 10^{-5} \text{ S cm}^{-1}$) is constant, which applies to the first and second coating, the annealed layer thickness is reduced from 1 μm to 0.86 μm . That average reduction of 0.14 μm during the second deposition seems plausible when ceramic particles partially plastically deform or blast out already annealed surface fragments. Especially when the thickness of the anchoring layer of PAD films on various substrates is considered to be $\approx 200 \text{ nm}$ and tends to lower values for harder substrate materials.^[18] The interaction depth of the new particles with the existing film can be determined to an average of 140 nm in this case. We suggest that during the entire coating process, a film build-up and a film removal process occurs where the incoming particles interact with the 100–200 nm thick surface layer of the substrate of the already deposited film. This process is mainly influenced by different kinetic energies of the impacting particles and the film/substrate hardness. It is pointed out that both the particle size distribution as well as the agglomeration and the particle velocity are critical parameters for the successful deposition.^[41,44] Agglomerates can absorb the released impact energy without creating sufficiently fresh surfaces as is necessary for film formation.^[52] A very narrow particle size distribution in the order of one micrometer (depending on the ceramic material) may have a positive effect on the deposition rate due to a reduced abrasive removal process. The coating quality and rate also depends on particle morphology and lattice defects, deposition parameters of the apparatus and internal layer stresses.

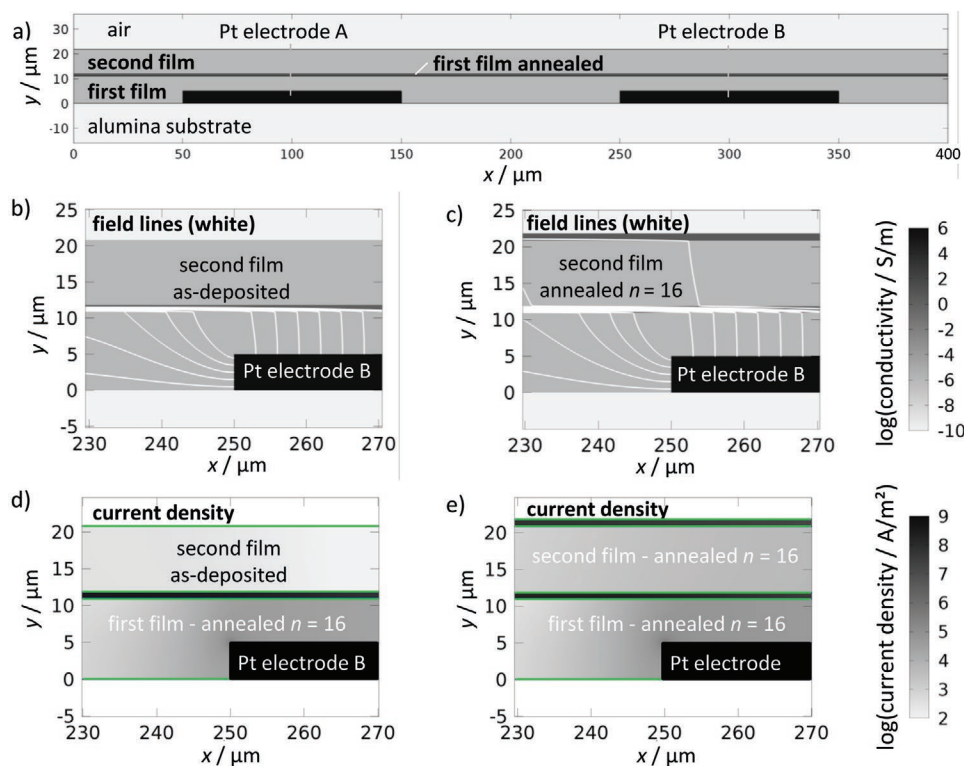


Figure 12. Model of the electrical behavior of a (12 + 10) μm thick PAD $\text{CuFe}_{0.98}\text{Sn}_{0.02}\text{O}_2$ film on interdigital electrodes (consisting of two subsequently sprayed films, wherein each was laser annealed after film formation): For the shown simulation, the lower first film is already annealed ($n = 16$), while the annealing state of the second film is varied: a) used 2D geometry; field line distribution near electrode B for b) an as-deposited second film and c) an annealed second film ($n = 16$); current densities in the identical region for d) an as-deposited second film and e) an annealed second film ($n = 16$) with green lines marking the boundaries of electrode and layers.

By the second laser-annealing, the overall resistance of the sample can be decreased further. The field lines are still located primarily within the first annealed layer (Figure 10 region b) that is close to the electrode B (Figure 12c); however, also an increased number of field lines pass the unaffected layer of the second coating (Figure 10 region c) up to its annealed surface layer (Figure 10 region d). The simulations of the current densities additionally prove this explanation. In Figure 12d, almost no charge transport is detected in the untreated second film (Figure 10 region c), but in the highly conductive intermediate layer (Figure 10 region b). When the surface of the second film up to a depth of 1 μm is laser-treated and becomes more and more conductive, an increasing number of electrons passes through the lower conductive yet thin layer (Figure 10 region c) and reaches the highly conductive new surface layer (Figure 10 region d).

The simulation again enables to separate the conductivity of the different layers in their as-deposited and annealed states. The conductivity of the three respectively four layers as a function of the numbers of laser scans is shown in Figure 13.

By annealing the first film ($n \leq 16$), the conductivity of the surface layer increases from 2.54×10^{-5} to $1.05 \times 10^{-2} \text{ S cm}^{-1}$, while the conductivity of the as-deposited bottom layer remains constant. Measured and simulated conductivity values match with the previous results from sample III in the two-layer setup. Laser-annealing of the subsequently applied second film also leads to an annealed layer at the surface with a high conductivity.

The second surface film has maximum conductivity of $1.70 \times 10^{-2} \text{ S cm}^{-1}$ after 16 scans. Nevertheless, the annealed surface conductivity is reduced compared to sintered bulk samples from literature.^[33] Since a reflex narrowing cannot be observed by XRD, the laser-based annealing may differ to a conventional annealing inside a furnace. Also, the microstructure of the annealed surface

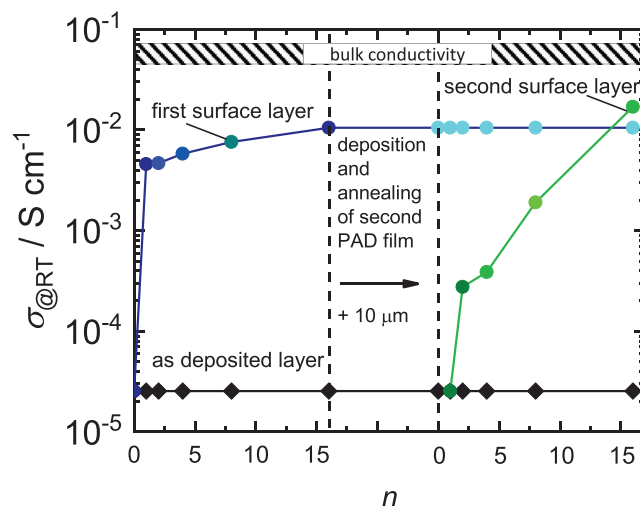


Figure 13. Calculated conductivity of the as-deposited film as well as the first surface layer and the second surface layer in dependence of the number of scans n compared to bulk samples from ref. [15].

film could not be taken into account for the simulation. The high cooling rate might result in a glassy surface layer structure. This hypothesis may explain an increased conductivity while the XRD pattern of the film does change during annealing.

5. Conclusion

The powder aerosol deposition method is a powerful tool to produce nanocrystalline ceramic films at room temperature on different surfaces like metals, glasses, polymers or ceramics with a thickness of several micrometer with an excellent bonding to the substrate. PAD even allows the deposition of moisture sensitive powders without the use of liquids in a scalable vacuum process. Despite these advantages, a thermal treatment after the deposition process is necessary to regain bulk-like functional properties. This can be a major drawback on the pathway to commercial industrialization when a furnace has to be used. There, the thermal annealing of films on low-melting substrates, for example, polymers is not possible. Also, the elevated temperature can cause unintended interdiffusion reactions between the substrate and the film.

In this work, we investigated the influence of laser irradiation with a wavelength of 355 nm on a nanocrystalline thermoelectric CuFeO_2 -PAD film. The focus of the work was on the microstructure of the film and on its electric conductivity.

Based on the short wavelength, the thermal penetration depth of the Nd:YAG laser in the nanocrystalline $\text{CuFe}_{0.98}\text{Sn}_{0.02}\text{O}_2$ layer is around one micrometer and therefore primarily affects the film surface. The high energy density of the laser causes a locally-selective melting of the surface film. High cooling rates lead to the formation of a surface layer with fine cracks, whereas no microstructural changes occur in the film below as well as in the contact area to the substrate.

Furthermore, the electrical conductivity of the annealed layer is increased significantly by the laser radiation. Simulations based on impedance spectra allow to quantify the surface conductivity, which is increased by three orders of magnitude from $1.67 \cdot 10^{-5} \text{ S cm}^{-1}$ in the as-deposited state to $1.03 \cdot 10^{-2} \text{ S cm}^{-1}$ after the laser-annealing.

Besides the proof that a new deposition on a heat-treated surface is possible, we postulate a continuous build-up and removal of the film during the deposition with an interaction depth of 100–200 nm between the impacting particles and the substrate based on the measurement data and the simulations. It may be of interest for future works to use the annealing process on thermally sensitive substrates so that the laser-based heat treatment can develop its full potential.

Supporting Information

Supporting Information is available from the Wiley Online Library or from the author.

Acknowledgements

Funding from the Deutsche Forschungsgemeinschaft (DFG, grant MO-1060/37-1) is gratefully acknowledged. Furthermore, the

authors are indebted to Angelika Mergner and the Bavarian Polymer Institute (BPI) for SEM imaging, as well as to the Department of Metal and Alloys (Prof. Uwe Glatzel) for the XRD measurements. The authors are grateful to Kira Schlesier for conducting the laser experiments.

Open access funding enabled and organized by Projekt DEAL.

Conflict of Interest

The authors declare no conflict of interest.

Keywords

post-deposition laser-annealing, powder aerosol deposition, room temperature impact consolidation, thermoelectric films

Received: June 22, 2020

Revised: August 25, 2020

Published online: October 5, 2020

- [1] J. Akedo, *J. Am. Ceram. Soc.* **2006**, *89*, 1834.
- [2] J. Akedo, J. Ryu, D.-Y. Jeong, S. D. Johnson, in *Advanced Piezoelectric Materials*, Vol. 2 (Ed: K. Uchino), Woodhead Publishing, Cambridge **2017**, Ch. 2.
- [3] C. Lee, J. Kim, H. Park, J.-s. Nam, K. S. Son, Y. T. Im, J. W. Lee, B. G. Chung, *Korean J. Met. Mater.* **2016**, *54*, 15.
- [4] Y. Liu, Y. Wang, X. Suo, Y. Gong, C.-J. Li, H. Li, *Ceram. Int.* **2016**, *42*, 1640.
- [5] D.-M. Chun, J.-O. Choi, C. S. Lee, S.-H. Ahn, *Surf. Coat. Technol.* **2012**, *206*, 2125.
- [6] M. Schubert, N. Leupold, J. Exner, J. Kita, R. Moos, *J. Therm. Spray Technol.* **2018**, *27*, 870.
- [7] J. Exner, P. Fuierer, R. Moos, *J. Am. Ceram. Soc.* **2015**, *98*, 717.
- [8] J. Exner, T. Nazareus, J. Kita, R. Moos, *Int. J. Hydrogen Energy* **2020**, *45*, 10000.
- [9] J.-J. Choi, K.-S. Cho, J.-H. Choi, J. Ryu, B.-D. Hahn, J.-W. Kim, C.-W. Ahn, W.-H. Yoon, J. Yun, D.-S. Park, *Mater. Lett.* **2012**, *70*, 44.
- [10] J. Exner, H. Pöpke, F.-M. Fuchs, J. Kita, R. Moos, *Materials* **2018**, *11*, 2072.
- [11] D. Hanft, J. Exner, R. Moos, *J. Power Sources* **2017**, *361*, 61.
- [12] M. Schubert, D. Hanft, T. Nazareus, J. Exner, M. Schubert, P. Niek, P. Glosse, N. Leupold, J. Kita, R. Moos, *Funct. Mater. Lett.* **2019**, *12*, 1930005.
- [13] P. Niek, J. Kita, M. Häming, R. Moos, *Materials* **2019**, *12*, 487.
- [14] P. Fuierer, R. Calvo, G. Stöbel, *Addit. Manuf.* **2020**, *35*, 101304.
- [15] T. Stöcker, J. Exner, M. Schubert, M. Streibl, R. Moos, *Materials* **2016**, *9*, 227.
- [16] N. H. Khansur, U. Eckstein, L. Benker, U. Deisinger, B. Merle, K. G. Webber, *Ceram. Int.* **2018**, *44*, 16295.
- [17] D. Hanft, J. Exner, M. Schubert, T. Stöcker, P. Fuierer, R. Moos, *J. Ceram. Sci. Technol.* **2015**, *6*, 147.
- [18] M. Schubert, M. Hahn, J. Exner, J. Kita, R. Moos, *Funct. Mater. Lett.* **2017**, *10*, 1750045.
- [19] J. Akedo, *J. Therm. Spray Technol.* **2008**, *17*, 181.
- [20] J. Akedo, *J. Ceram. Soc. Jpn.* **2020**, *128*, 101.
- [21] J. Exner, J. Kita, R. Moos, *J. Mater. Sci.* **2019**, *54*, 13619.
- [22] P. Sarobol, M. Chandross, J. D. Carroll, W. M. Mook, D. C. Bufford, B. L. Boyce, K. Hattar, P. G. Kotula, A. C. Hall, *J. Therm. Spray Technol.* **2016**, *25*, 82.
- [23] J. Exner, T. Nazareus, D. Hanft, J. Kita, R. Moos, *Adv. Mat.* **2020**, *32*, 1908104.
- [24] S. Baba, H. Tsuda, J. Akedo, *IEEE Trans. Ultrason. Ferroelectr. Freq. Control* **2008**, *55*, 1009.

- [25] S. Baba, J. Akedo, *J. Am. Ceram. Soc.* **2005**, *88*, 1407.
- [26] S. Baba, J. Akedo, *Appl. Surf. Sci.* **2009**, *255*, 9791.
- [27] S. Baba, J. Akedo, M. Tsukamoto, N. Abe, *J. Am. Ceram. Soc.* **2006**, *89*, 1736.
- [28] H. Palneedi, I. Choi, G.-Y. Kim, V. Annapureddy, D. Maurya, S. Priya, J.-W. Kim, K. J. Lee, S.-Y. Choi, S.-Y. Chung, S.-J. L. Kang, J. Ryu, *J. Am. Ceram. Soc.* **2016**, *99*, 2680.
- [29] H. Palneedi, D. Maurya, G.-Y. Kim, S. Priya, S.-J. L. Kang, K.-H. Kim, S.-Y. Choi, J. Ryu, *Appl. Phys. Lett.* **2015**, *107*, 012904.
- [30] H. Palneedi, D. Maurya, G.-Y. Kim, V. Annapureddy, M.-S. Noh, C.-Y. Kang, J.-W. Kim, J.-J. Choi, S.-Y. Choi, S.-Y. Chung, S.-J. L. Kang, S. Priya, J. Ryu, *Adv. Mat.* **2017**, *29*, 1605688.
- [31] T. Shinonaga, *J. Laser Micro/Nanoeng.* **2014**, *9*, 204.
- [32] T. Shinonaga, M. Tsukamoto, A. Nagai, K. Yamashita, T. Hanawa, N. Matsushita, G. Xie, N. Abe, *Appl. Surf. Sci.* **2014**, *288*, 649.
- [33] M. Tsukamoto, N. Abe, Y. Soga, M. Yoshida, H. Nakano, M. Fujita, J. Akedo, *Appl. Phys. A* **2008**, *93*, 193.
- [34] T. Nozaki, K. Hayashi, T. Kajitani, *J. Electron. Mater.* **2009**, *38*, 1282.
- [35] T. Stöcker, R. Moos, *Materials* **2018**, *11*, 1888.
- [36] K. P. Ong, K. Bai, P. Blaha, P. Wu, *Chem. Mater.* **2007**, *19*, 634.
- [37] J. Exner, R. Moos, presented at Dresdner Sensor-Symp., Dresden, Germany, December **2015**.
- [38] E. Mugnier, A. Barnabe, P. Tailhades, *Solid State Ionics* **2006**, *177*, 607.
- [39] C. Ruttanapun, B. Boonchom, M. Thongkam, S. Kongtaweelert, C. Thanachayanont, A. Wichainchai, *J. Appl. Phys.* **2013**, *113*, 023103.
- [40] M. Schubert, J. Exner, R. Moos, *Materials* **2014**, *7*, 5633.
- [41] J. Exner, M. Schubert, D. Hanft, J. Kita, R. Moos, *J. Eur. Ceram. Soc.* **2019**, *39*, 592.
- [42] H.-Y. Chen, G.-W. Fu, *Appl. Surf. Sci.* **2014**, *288*, 258.
- [43] K. Naoe, M. Nishiki, K. Sato, *J. Therm. Spray Technol.* **2014**, *23*, 1333.
- [44] H. Kwon, Y. Kim, H. Park, S. Jeong, C. Lee, *Ceram. Int.* **2020**, *46*, 9016.
- [45] D.-W. Lee, H.-J. Kim, Y.-H. Kim, Y.-H. Yun, S.-M. Nam, *J. Am. Ceram. Soc.* **2011**, *94*, 3131.
- [46] L.-S. Wang, H.-F. Zhou, K.-J. Zhang, Y.-Y. Wang, C.-X. Li, X.-T. Luo, G.-J. Yang, C.-J. Li, *Ceram. Int.* **2017**, *43*, 4390.
- [47] P. Dordor, J. P. Chaminade, A. Wichainchai, E. Marquestaut, J. P. Doumerc, M. Pouchard, P. Hagenmuller, A. Ammar, *J. Solid State Chem.* **1988**, *75*, 105.
- [48] H. Nasu, M. Hasegawa, T. Hashimoto, A. Ishihara, K. Fujita, K. Tanaka, *J. Ceram. Soc. Jpn.* **2015**, *123*, 448.
- [49] N. H. Khansur, U. Eckstein, Y. Li, D. A. Hall, J. Kaschta, K. G. Webber, *J. Am. Ceram. Soc.* **2019**, *102*, 5763.
- [50] J. Kim, J. I. Lee, D. S. Park, E. S. Park, *J. Appl. Phys.* **2015**, *117*, 014903.
- [51] J. Akedo, J.-H. Park, Y. Kawakami, *Jpn. J. Appl. Phys.* **2018**, *57*, 07LA02.
- [52] J. Exner, M. Hahn, M. Schubert, D. Hanft, P. Fuierer, R. Moos, *Adv. Powder Technol.* **2015**, *26*, 1143.